ACS Photonics

Article

pubs.acs.org/journal/apchd5

Fast Modulation of Terahertz Quantum Cascade Lasers Using Graphene Loaded Plasmonic Antennas

Riccardo Degl'Innocenti,*[,†] David S. Jessop,[†] Christian W. O. Sol,[†] Long Xiao,[†,‡] Stephen J. Kindness,[†] Hungyen Lin,[§,∥] J. Axel Zeitler,[§] Philipp Braeuninger-Weimer,[‡] Stephan Hofmann,[‡] Yuan Ren,[†] Varun S. Kamboj,[†] Jonathan P. Griffiths,[†] Harvey E. Beere,[†] and David A. Ritchie[†]

[†]Cavendish Laboratory, University of Cambridge, J. J. Thomson Avenue, Cambridge CB3 0HE, United Kingdom

[‡]Department of Engineering, University of Cambridge, J. J. Thomson Avenue, Cambridge CB3 0FA, United Kingdom

[§]Department of Chemical Engineering and Biotechnology, University of Cambridge, Pembroke Street, Cambridge CB2 3RA, United Kingdom

[∥]Department of Engineering, Lancaster University, Lancaster LA1 4YW, United Kingdom

Supporting Information

ABSTRACT: We report the fast amplitude modulation of a quantum cascade laser emitting in single-mode operation in the terahertz frequency range by employing compact, integrated devices based on the interplay between plasmonic antenna arrays and monolayer graphene. By acting on the carrier concentration of graphene, the optical response of these plasmonic resonances was modified. The modulator's characteristics have been studied by using both time domain spectroscopic laser systems, yielding the broad frequency response of these resonant arrays, and quantum cascade lasers, providing us with a narrow and stable laser source, a mandatory prerequisite for the determination of the modulation speed of these devices. The measured modulation speed exhibits a cutoff frequency of 5.5 MHz ± 1.1 MHz. These results represent the first step toward the realization of fast integrated circuitry for communications in the terahertz frequency range.

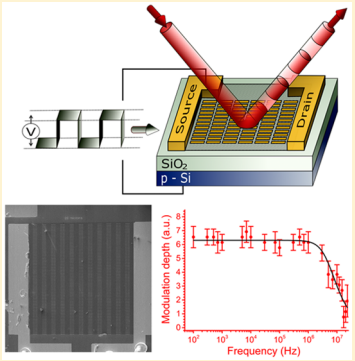

KEYWORDS: *terahertz optical modulator, graphene, plasmonic antennas, quantum cascade lasers*

Recently, an impressive advancement has been achieved by terahertz (THz) solid-state sources in terms of performance with the quantum cascade laser (QCL)[1,2] and by time-domain spectroscopic (TDS) systems, in terms of costs, compactness, and bandwidth. However, the lack of suitable optoelectronic devices, both passive and active, has so far hindered technology in this spectral region from reaching its full potential in many demanding sectors, such as spectroscopy or communications. The realization of a tunable external THz amplitude/phase/frequency modulator would allow for fast reconfigurable spectroscopic systems to be implemented for amplitude, frequency, or phase stabilization.[3] Terahertz communications represent a fast evolving research area. Wireless communications always strive for broader bandwidths, and the THz range represents a nonallocated frequency range. Additionally, because of the high carrier frequency, THz radiation has the potential to yield high transmission rates, as high as 100 Gbit s^{-1}, as recently demonstrated in the sub-THz frequency range.[4] The basic optical building blocks for a complex THz communications system consist in components such as amplitude/phase modulators, beam steering devices, and phase arrays, which are capable of fast reconfiguration rates. Research in THz optoelectronics based on graphene[5] is fast gaining popularity because of their fundamental importance at these frequencies where natural occurring materials have a poor electromagnetic response and because of the promise of the implementation of the unique graphene properties into innovative and more performant devices. Plasmonic and metamaterial[6−10] devices have already established themselves as a versatile tool for the creation of efficient and compact devices in the mid-infrared/terahertz spectral range for spectroscopic applications,[11−13] modulation,[14−18] emission and detection,[19−22] and more fundamental physical studies.[23,24]

These devices, which exploit the extreme subwavelength light concentration of the surface polaritons to boost the light−matter interaction, are normally engineered as metallic features over a positive dielectric constant substrate. The amplitude modulation of THz radiation with hybrid metamaterial−graphene architectures by using ultralow bias[25,26] or high magnetic fields[27] was recently investigated. Further, a graphene-based modulator integrated on a QCL was demonstrated with remarkable performance.[28] However, the realization of an external fast modulator capable of efficiently modulating terahertz radiation from a QCL has not been demonstrated yet. Such a device, in fact, would uniquely address the need of

Received: November 23, 2015
Published: February 23, 2016

DOI: 10.1021/acsphotonics.5b00672
ACS Photonics 2016, 3, 464−470

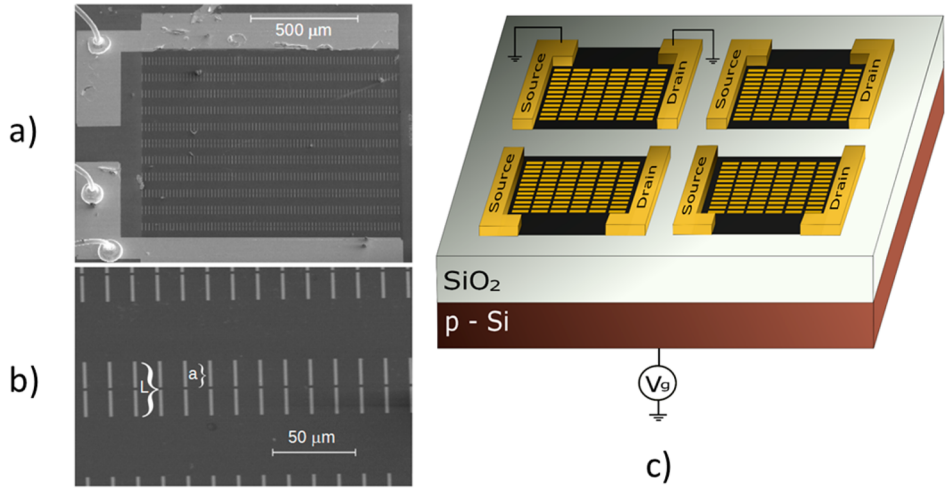

Figure 1. SEM picture (a) of an array of the final device and (b) a detail of the same array. The graphene area, contacted by source and drain metallic pads, is clearly distinguishable. The total antenna length L is equal to $2a + w$, where the distance between the two parts of the antenna w has been kept fixed to 2 μm for all the arrays, and a is the antenna arm length. The width of the metal features was always kept equal to 2 μm. The pitch along the antennas' direction was 1.55·L, and fixed to 16 μm in the other direction. (c) Schematic of the final device which integrates four independent arrays each characterized by a different total length L equal to 42, 46, 50, and 54 μm.

independently operating source and modulator and provide a fundamental and versatile tool in light of spectroscopic experimental arrangements, in addition to being compatible with multiple sources. Fast external terahertz modulators have been realized by implementing two-dimensional electron gas (2DEG) with a modulation speed up to 2 MHz[29] or incorporating high electron mobility transistors in a metamaterial device[30] with a modulation cutoff frequency of about 10 MHz. Lately, an increasing number of experiments have been focused on the realization of graphene-based terahertz modulators because of its remarkable properties, such as the wide carrier concentration modulation range. The modulation speed has significantly increased from the 20 kHz of the first devices,[14] to the 12.6 MHz achieved in a complex metamaterial graphene integrated modulator.[15] In our approach, comparable modulation speeds were achieved but in a simpler configuration. In addition, the system has been tested also with a THz quantum cascade laser, thus paving the way to the implementation of this powerful and spectrally narrow source in spectroscopic and communication applications.

In this manuscript, we aim to investigate the reconfiguration speed of amplitude modulators operating in the THz frequency range based on the interplay of plasmonic antenna arrays and graphene. These results represent an important milestone toward the realization of a fast, integrated platform for THz communications. At the same time, the present work opens the way to new efficient routes aimed at the amplitude/frequency modulation of THz sources, thus finding applications in diverse research areas (e.g., spectroscopy).

In order to achieve an active optical device, plasmonic antenna arrays were fabricated on top of a transferred graphene monolayer with a procedure similar to refs 25,26. The coupling of these resonant elements with graphene allows the modification of the whole of the device's optical response, by acting on the graphene carrier concentration. In analogy to electronic circuits, the gating of graphene results in a modified load impedance. Following the electrical characterization of the graphene, in particular the determination of the position of its Dirac point, the samples were tested with both a broadband THz-TDS system and a narrow-frequency QCL. While the first approach yields the broad frequency response of the device for different values of the graphene conductivity, the implementation of a powerful and stable single frequency QCL source, allows the determination of the modulation speed of the device, which is found to be in the MHz range.

RESULTS AND DISCUSSION

Graphene growth and transfer is described in the Methods section together with the sample fabrication. Figure 1a,b show scanning electron microscopy (SEM) images of an array of the final device. The final device integrates four different arrays on the same sample, each composed of identically sized plasmonic antennas, as shown in Figure 1c, each characterized by a different total length L equal to 42, 46, 50, and 54 μm. The antenna size unit was scaled in the different arrays to have a frequency response approximately covering the range between 2 THz and 3 THz, where both THz−TDS and THz QCLs overlap. The device is then mounted on a chip carrier and wire bonded for electrical testing. The pitch, the distance between neighboring antennas, has been kept fixed to 1.55 times the total length L along the antenna direction and to 16 μm along the perpendicular one. In order to excite the plasmonic resonances of these antennas the length a, as shown in Figure 1b, should correspond to $\sim m \cdot \lambda_{sp}/2 \cdot n_{eff}$ where λ_{sp} is the vacuum wavelength of the resonant radiation, n_{eff} is the effective refractive index of the plasmonic mode supported by the metal feature, and m is an odd integer number. A more detailed simulation, however, is required to better investigate and disentangle the optical response of the graphene-loaded plasmonic antennas and the response of the graphene alone. The Dirac points of the graphene layers were determined for each sample using two Keithley source/measure units (Model 2400), the first of which provided a constant current of 5 μA to the source/drain while the second provided a variable bias to the back gate contact (−40 to 120 V). A typical example of the electrical characterization is shown in Figure 2 for the samples with a = 24 μm and a = 26 μm, corresponding to the full and dotted black line, respectively. The leakage current toward the gate was below 10 nA for all samples, as also reported in Figure 2. The Dirac points of all the samples were found between 90

DOI: 10.1021/acsphotonics.5b00672
ACS Photonics 2016, 3, 464−470

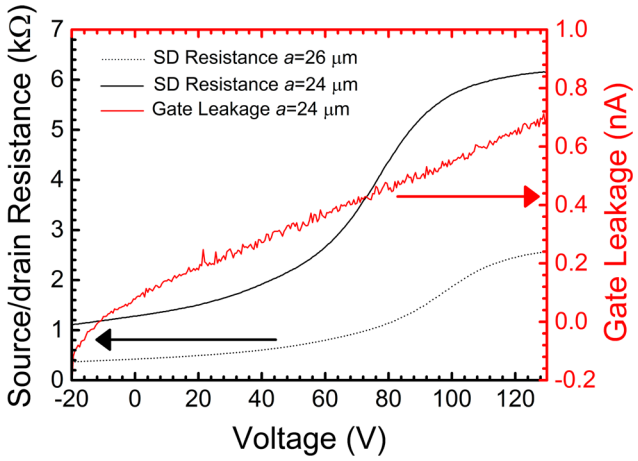

Figure 2. Black curves report the typical source/drain resistance plots of the arrays similar to what is shown in Figure 1, having an a value of 26 and 24 μm, respectively. These data, as indicated by the black arrow, are reported on the bottom-left layer axis. The red curve represents the gate leakage for the 26 μm array, with the corresponding curve for the 24 μm being almost identical. These values, as indicated by the red arrow, are reported in the top-right layer axis.

and 140 V, which is compatible with p-doped chemical vapor deposition (CVD) grown graphene. The source/drain resistances in all the samples were observed to be between 0.4 and 7 kΩ. These resistance values include also the contributions of the metallic antennas and contacts. Because the metallic features in the arrays introduce periodic parallel paths with different impedance for the current flow, the resistances measured cannot be attributed solely to the graphene carrier concentration and cannot be correlated directly to the graphene resistivity. However, these measurements provide the voltage characteristics which are needed for the optical measurements and yield a range in the device conductivity which, even though overestimated, can be implemented in the finite element simulations.

The commercial software Comsol Multiphysics(R) v. 5.0 was used to simulate the unit cell of our device. The graphene monolayer was modeled in the finite element based software by expanding its thickness to an artificial value of 15 nm. The dc conductivities were inferred from the electrical characterization of the different arrays. In the framework of the Drude model, these values were used to model the complex conductivity σ of graphene at different gate biases with a procedure similar to that reported in ref 24. The conductivity σ is then related to the dc conductivity σ_0 through the relation $1/\sigma = (1 - i\cdot\omega\tau)/\sigma_0$ where the scattering time τ was assumed to be 15 fs[15] and ω is the angular frequency. Figure 3a shows, for a xy slice of the unit cell having a length of 1.55·L and a width of 16 μm, the normalized electric field at resonance for the array having a = 26 μm in the case of no damping (e.g., zero graphene conductivity). As can be seen, the mode intensity has a maximum value at the ends of the antennas, in agreement with the condition $m\cdot\lambda_{sp}/2\cdot n_{eff}$ with m = 1. Further simulations are reported in the Supporting Information in Figure 1 SI. The device was tested with a commercially available THz pulsed imaging system Imaga 2000 from TeraView (Cambridge, U.K.), based on biased photoconductive antennas and yielding the broad-band frequency response of the antennas arrays. The experimental procedure follows closely to that previously reported in ref 3. The reflected electric field was recorded at different spatial coordinates with a step size of 100 μm and keeping the sample in the focus of the system, which has a resolution of ∼200 μm. The reflected THz radiation from the different arrays was monitored for different back-gate biases with the polarization fixed along the longitudinal direction of the plasmonic antennas. The peak electric field reflected from the sample at different positions yields thus a THz map, similar to the one shown in Figure 3b. From these acquired data, it is possible to extrapolate the reflected intensity from these arrays, showing a broad peak in correspondence of the plasmonic resonance. The experimental results for the array with a = 26 μm are shown in Figure 3c for different gate bias voltages. By increasing the graphene carrier concentration/conductivity, the resonant plasmonic mode is more attenuated. As expected, for higher values of graphene film conductivity, the resonances are red-shifted. Depending on the voltage bias applied, the resonance peaks at 2.1−2.3 THz. The results are in close agreement with the simulations presented in the Supporting Information. In particular, it is possible to observe a distinct resonance shift of about 200 GHz between the resonance for 0 and 120 V, as predicted by the simplistic model. This is attributed to the combined effect of the increased reflectivity of

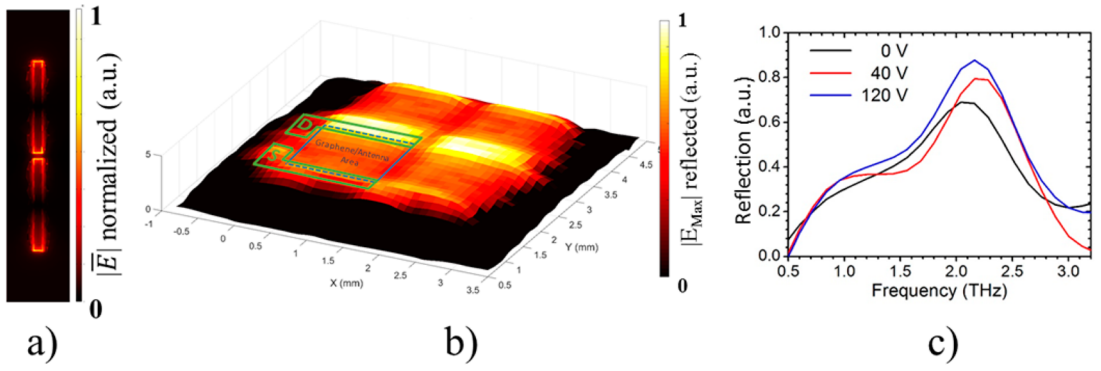

Figure 3. (a) Normalized calculated E-field at a resonant frequency around 2.3 THz for the a = 26 μm array device simulated with zero conductivity. The maximum of the E-field, calculated in a xy slice 100 nm above the metal features, lies in the center of the antennas. (b) The measured reflection spectra of the E-field $|E_{Max}|$ recorded for different positions of the sample, always kept in the focus of the system provides a THz map of the four arrays. (c) The frequency response of the a = 26 μm array at different gate voltages is obtained from TDS measurements similar to the one shown in (b). These broad resonances are damped and blue-shifted at higher gate voltages (e.g., lower carrier concentrations).

DOI: 10.1021/acsphotonics.5b00672
ACS Photonics 2016, 3, 464−470

graphene for high conductivity values and reduced plasmonic resonance strength.

In order to test the modulation speed of the device, a more powerful, stable, and narrow frequency THz source is required. A bound to continuum quantum cascade laser was used for all these measurements. The QCL emits at 2.05 THz in single mode around the maximum current density, which is a fundamental feature required in order to test the speed performance of these amplitude modulators. In fact, single-mode operation is required in order to avoid laser mode hopping which would translate in a laser amplitude modulation. Correspondingly, this would affect the data interpretation because of the convolution of different modes, each characterized by a distinct frequency and power, with the plasmonic resonances. The emission frequency overlaps significantly with the plasmonic resonances for a = 26 μm and partly also for the a = 24 μm plasmonic antenna arrays. A general schematic drawing of the experimental setup is shown in Figure 4. QCL radiation is collimated with a parabolic mirror

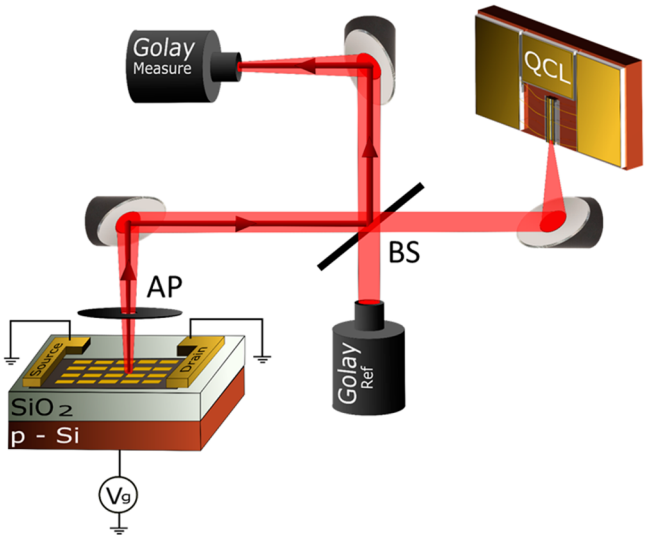

Figure 4. Schematic of the setup used for the modulation speed. BS is a highly resistive, low-temperature-grown GaAS double side polished wafer acting as a beam splitter, and AP is a 1 mm diameter aperture place as close as possible to the modulator.

and after a beam splitter is partly focused onto the device with another parabolic mirror, which has a focal length of 2.5 cm and is partly focused on a Golay cell detector in order to monitor the stability of the power source. Another parabolic mirror focuses the light reflected from the sample to a second Golay cell, which was used to measure the reflectivity modulation. The first experiment aimed to demonstrate the modulation of the THz light emitted from the QCL. A schematic of the experimental setup is shown in Figure 4. In this configuration, the QCL laser was operating in continuous pulse mode, with a 30% duty cycle and 100 kHz repetition rate at maximum power current density. The optical modulator source and drain contacts were grounded, and a voltage bias was applied to the gate. The DC bias applied to the gate spanned from −40 to 120 V, which set the working point, and an AC slow modulation (7 Hz frequency), consisting in a 0−10 V square-wave modulation added to this DC value. The reflected power was then focused to the Golay cell and demodulated by a lock-in amplifier having the AC modulation frequency as reference. A pinhole with a 1 mm diameter was positioned in front of the graphene modulator to ensure that the illuminated area was at most the same as the device array area and that all the light reflected was coming from the array of interest. A second Golay cell was implemented to monitor the stability of the QCL emitted power through the measurements and rule out cases of mode hopping. A typical example of the measurements is reported in Figure 5 for the a = 26 μm and a = 24 μm arrays corresponding

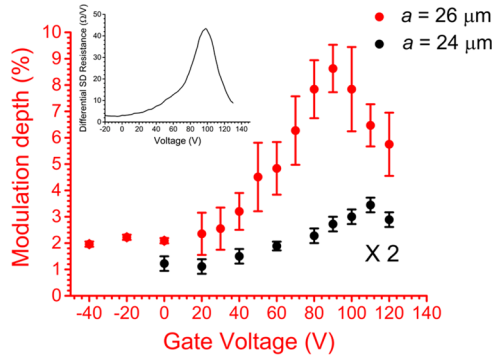

Figure 5. Modulation depth for various DC gate voltage applied for the arrays having a = 26 μm and a = 24 μm, corresponding to red circles and black circles, respectively. The AC modulation consisted of a 7 Hz TTL signal with an amplitude of 0−10 voltage which was added to the DC component. The maximum modulation depth is achieved at 90 V for the array with a = 26 μm consistent with the maximum value of the differential resistance of the array, reported in the inset.

to red and black symbol points, respectively. The total peak power impinging to the array was calculated to be 65 μW for the first array and 157 μW for the second one. The modulation depth for the first array increases with increasing gate voltage, peaking around 90 V reaching a maximum of ∼8.6% and then starts reducing again. This trend was expected because by changing the working point, the maximum conductivity modulation is reached around 100 V. The differential resistivity of the device is reported in the inset of Figure 5 for clarity and is consistent with the modulation depth measurements. Measurements performed with the a = 24 μm array revealed a similar trend but with a reduced modulation depth of only 1.6%. Even though the extent of the sheet resistivity modulation of graphene for this array was larger, as shown in Figure 2, the final QCL modulation depth was lower because of the reduced overlap of the plasmonic resonance with the laser frequency in good agreement with the simulations performed with Comsol Multiphysics and reported in Figure 1 SI in the Supporting Information. Finally, the sample was rotated by 90° such that the polarization was not exciting the plasmonic resonances in order to appreciate the graphene stand-alone modulation depth. The modulation depth could not be observed within the noise of the measurements. Another device was realized without any metal plasmonic antennas on top in order to perform a comparison with a pure graphene modulator, ruling out any effect introduced by further fabrication steps. The device exhibited maximum source-drain resistance an order of magnitude higher than in the other samples and Dirac point around 70 V but did not show any appreciable modulation depth above the noise floor. This demonstrates that the modulation of the conductivity in graphene alone does not yield any appreciable power modulation depth in these experiments. Conversely, when boosted by plasmonic reso-

DOI: 10.1021/acsphotonics.5b00672
ACS Photonics 2016, 3, 464−470

nances, the contribution to the total modulation given by the graphene Drude response is not negligible, coherent with Figure 5.

Testing the device modulation speed, which is expected to be above hundreds of kHz, with a Golay cell detector, which is usually sensitive only to frequencies lower than 100 Hz, was accomplished with a different detection scheme, shown in Figure 6. Our approach is similar to what has been developed in

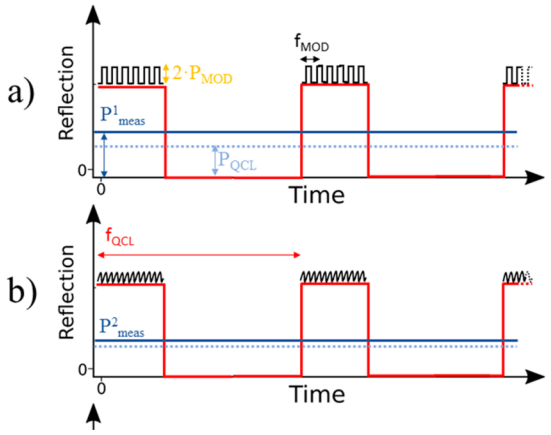

Figure 6. Experimental scheme implemented for the determination of the modulation speed of these devices. A TTL voltage wave is applied to the QCL with low-frequency f_{QCL}. The fast modulation f_{MOD} is applied to the device superimposed onto a DC high-voltage bias which determines the working point. The reflection signal coming from the sample is detected by a Golay cell and is then demodulated by a lock-in amplifier having the frequency f_{QCL} as reference. The total signal detected is P1 meas for low frequencies (a), is then reduced to P2 meas at high frequencies (b), and lastly, when the device cannot follow the modulation (c), the reflectivity is given by P3 meas.

parallel and recently reported in ref 28. The laser was modulated with a frequency f_{QCL} of 22 Hz in continuous pulse mode, 30% duty cycle and at the current density corresponding to maximum output power. A modulation frequency f_{MOD} was applied to the device with modulation depth of 10 V by using a 30 MHz function generator from Stanford Research system model DS345. A lock-in amplifier, having f_{QCL} as a reference signal, demodulated the reflection coming from the device. For sufficiently low f_{MOD} frequencies, as shown in Figure 6a, the power detected by the Golay cell was P^1_{meas}, which is the sum of the QCL reflected power P_{QCL} plus half of the superimposed power modulation given by the device, P_{MOD}. Since f_{MOD} is too fast to be detected by the Golay cell, the contribution to the total reflectivity will be the average value of the fast modulated reflectivity. At higher frequencies, as shown in Figure 6b, the device is unable to follow the modulation, and therefore, the total power seen by the lock-in was reduced to P^2_{meas}, with $P^1_{meas} > P^2_{meas}$ because P_{MOD} is reduced. Finally, Figure 6c, the modulation signal was too fast to be followed by the modulator, and the total reflected power is P^3_{meas}, which is simply given by P_{QCL}. The amplitude modulator behaves as a low pass filter being limited by both its RC time constant and the electronics driving it, with the latter considered negligible. The modulation depth measurements, acquired with the device working point set to 100 V to detect the maximum modulation depth, are reported in Figure 7. The measurements have been acquired at different gate voltages of 70 and 100 V. In order to rule out the possibility of a drift of

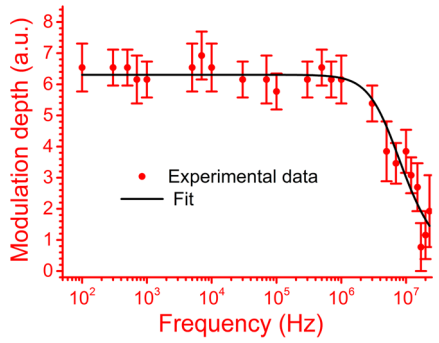

Figure 7. Modulation speed measurements. The QCL was driven in continuous pulse mode at 22 Hz and the fast modulation was applied to the modulator. The cutoff frequency for this measurement was 5.5 ± 1.1 MHz at a gate voltage of 100 V.

the optical system as possible cause of the reduction in the modulation depth observed at high frequencies, the set of measurements shown in Figure 7 was acquired chronologically from 500 kHz to the highest frequency, 20 MHz, and then from 300 kHz to the lowest one, 100 Hz. Similar acquisitions have been recorded after completely realigning the optical system and are shown in the Supporting Information presenting consistent values. The continuous line in Figure 7 represents the best fit using the standard formula for the capacitive low-pass filter having a transfer function of $1/(1 + (f/f_c)^2)^{1/2}$ where f is the modulation frequency and f_c the lowest 3 dB cutoff frequency of the filter. The cutoff frequency f_c was left as free fitting parameter. The results from the fitting procedure are reported in Table 1. Even though in principle it should be

Table 1. Results of the Fitting Procedure for Three Different Measurements for DC Gate Voltages of 70 and 100 V[a]

gate voltage (V)	cutoff frequency (MHz)
70	3.9 ± 1.1
100	5.5 ± 1.1
100*	4.1 ± 1.3

[a]The measurements have been performed after a complete realignment of the system each time. In order to rule out possible drifts, the acquisition at 70 V has been performed from the lowest frequency to the highest one. The set of measurements at 100 V, also shown in Figure 7, was recorded in two acquisition steps: the first one from 500 kHz to the highest frequency and the second from 300 kHz to the lowest one. Finally, the measurement at 100 V* was acquired from the highest frequency to the lowest one. The plots at 70 V and at 100 V* are reported in the Supporting Information.

possible to appreciate the differences in modulation depths and in cutoff frequencies at different gate biases, the limitations of these measurements due to their accuracy and reproducibility prevent such comparison. The highest cutoff frequency f_c for this modulator was found to be 5.5 MHz ± 1.1 MHz, as shown in Figure 7. The procedure schematically reproduced in Figure 6 represents a simplified picture. In fact, because the Golay cell is sensitive only to slow frequency power differences, the fast reflectivity modulation superimposed on top of the reflectivity given by the sample is only seen as an average value. Because the transfer function between the gate voltage applied to the sample and the reflectivity detected by the Golay cell is nonlinear, the average values seen by the Golay at low and high frequencies differs significantly and allowed the determination of the cutoff frequency. Because the transfer function is

DOI: 10.1021/acsphotonics.5b00672
ACS Photonics 2016, 3, 464−470

unknown and the development of an equivalent circuital model capable of describing the system is beyond the scope of this manuscript, a precise quantification of the modulation depths cannot be inferred from the fast modulation speed measurements. The limit in the modulation depth, shown in Figure 5, is attributed mainly to the finite AC voltage applied. The modulation depth can be increased by increasing the AC voltage applied or by optimizing the device architecture. Atmospheric adsorbants have been found to p-dope graphene films and cause a shift in the Dirac point. This can be prevented by encapsulating the graphene film (e.g., with Al_2O_3),[31] such that the Dirac point can be achieved with low biases, thus allowing the exploitation of the full range of conductivity available. This device architecture was optimized for high reconfiguration speeds, which is the key result of this work. Therefore, the highest resistance seen by the low pass filter is given by the graphene layer. The choice of having the graphene exposed was made in order to achieve the lowest resistance, thus allowing higher cutoff frequencies, at the expense of the modulation depth. An estimation of the theoretical performance of this device can be obtained in analogy with a low-pass frequency filter by developing a model similar to that reported in refs 17,28, where the parasitic effects produced by the contacts (parallel parasitic capacitance) have been taken into account and the resistance of the Si-substrate considered negligible. The capacitance C_{graph} of the graphene array area is given by the standard formula for the parallel plate capacitor $C_{graph} = \varepsilon_0\varepsilon_r \cdot A/d$, where ε_0 is the vacuum permittivity, ε_r the relative dielectric constant of SiO_2, A the total graphene area, and d the thickness of SiO_2 dielectric layer. Assuming a thickness d of 300 nm and a relative dielectric constant of 3.8, the capacitance is estimated to be ∼126 pF. From the model, a 3 dB cutoff frequency of 5.5 MHz ± 1.1 MHz should correspond to an effective graphene resistance R, which varies between 520 Ω and 920 Ω, in good agreement with the measured value for the a = 26 μm antenna array source/drain resistance, whose plot at different gate voltages is reported in Figure 2 and which takes into account also the graphene/contact resistances. The model is a first approximation of the complex transfer function between the voltage applied to the modulator, and its optical responsivity, but is useful in light of further optimizations.

The maximum modulation speed can be increased by reducing the size of the arrays. A reduction of the sample to a size comparable to the wavelength (e.g., 200 × 200 μm^2), a minimization of the contact pads area in order to reduce the parasitic capacitance, and a further optimization of the other resistances, should yield a higher cutoff frequency, beyond 100 MHz. The modulation depth could be improved as well by either encapsulating the graphene film, or implementing multiple independently tunable monolayer graphene stacks, with a double gate architecture, or denser packaging of the antennas in a sort of "superdipole" arrangement.

In conclusion, we have presented the realization of a compact, integrated optoelectronic device based on plasmonic antennas and graphene for the fast modulation of terahertz frequencies. The device has been modeled with both finite element methods and basic electronic circuital formulas showing a remarkable agreement with the experimental results acquired with broadband TDS systems and single-frequency quantum cascade laser emitting around 2 THz. A novel experimental technique has been developed in order to retrieve the cutoff frequency of these devices even at MHz modulation speed using slow-responding detectors, such as a Golay cell. This represents a significant progress compared to other more conventional techniques which allows a direct determination of the cutoff frequency but typically required cryogenic operating temperature (e.g., superconducting bolometers). The device tested present a cutoff frequency of 5.5 MHz ± 1.1 MHz, reproducible over several measurements. These results pave the way to the realization of a fast integrated optoelectronic class of devices for Terahertz communications.

METHODS

Graphene Growth and Transfer. Sample fabrication starts from the transfer of a monolayer graphene to a SiO_2/Si substrate (300 nm/525 μm thick) grown by chemical vapor deposition (CVD). The Si substrate was Boron-doped (∼20 Ω·cm) to allow gating of the device. The CVD graphene growth was performed on Cu foils (25 μm thick, Alfa Aesar purity 99.98%) using CH_4 as the precursor and PMMA (poly methylmethacrylate) as a support for the transfer followed by $FeCl_3$ chemical etching to remove the Cu.

Sample Fabrication. Four large graphene areas were defined with size of 1.2 × 1.2 mm^2 each, by using optical lithography and oxygen plasma etching. A second step of optical lithography, Ti/Au (10/120 nm) thermal evaporation and lift-off was used to fabricate the metallic contacts, thus realizing source and drain pads. The definition of the antennas was achieved by double layer electron beam lithography. The graphene underneath the exposed patterns was removed with oxygen dry etching. The final definition of the antennas has been achieved by a second step of metallic (Ti/Au, 10/80 nm) thermal evaporation and lift off. The sample is then cleaved, mounted on a chip carrier, and wire-bonded in order to perform the electrical characterization and the biasing.

ASSOCIATED CONTENT

Supporting Information

The Supporting Information is available free of charge on the ACS Publications website at DOI: 10.1021/acsphotonics.5b00672.

Simulation performed with the finite element commercial software Comsol Multiphysics; simulated terahertz reflection response of the device arrays and their frequency/amplitude response at different conductivity level of the graphene film; frequency response of the modulator at different gate bias working points (PDF)

AUTHOR INFORMATION

Corresponding Author

*E-mail: rd448@cam.ac.uk.

Notes

The authors declare no competing financial interest.

ACKNOWLEDGMENTS

R.D., Y.R., and H.E.B. acknowledge financial support from the Engineering and Physical Sciences Research Council (Grant No. EP/J017671/1, Coherent Terahertz Systems). H.L. and J.A.Z. would like to acknowledge the financial support from UK EPSRC Research Grant EP/L019922/1. S.H. acknowledges funding from EPSRC (Grant No. EP/K016636/1, GRAPHTED). Additional data sets related to this publication are available from the Cambridge University data repository at https://www.repository.cam.ac.uk/handle/1810/253983.

DOI: 10.1021/acsphotonics.5b00672
ACS Photonics 2016, 3, 464−470

REFERENCES

(1) Köhler, R.; Tredicucci, A.; Beltram, F.; Beere, H. E.; Linfield, E. H.; Davies, A. G.; Ritchie, D. A.; Iotti, R. C.; Rossi, F. Terahertz semiconductor-heterostructure laser. *Nature* **2002**, *417*, 156−159.

(2) Sirtori, C.; Barbieri, S.; Colombelli, R. Wave engineering with THz quantum cascade lasers. *Nat. Photonics* **2013**, *7*, 691−701.

(3) Ren, Y.; Hayton, D. J.; Hovenier, J. N.; Cui, M.; Gao, J. R.; Klapwijk, T. M.; Shi, S. C.; Kao, T.-Y.; Hu, Q.; Reno, J. L. Frequency and amplitude stabilized terahertz quantum cascade laser as local oscillator. *Appl. Phys. Lett.* **2012**, *101*, 101111.

(4) Koenig, S.; Lopez-Diaz, D.; Antes, J.; Boes, F.; Henneberger, R.; Leuther, A.; Tessmann, A.; Schmogrow, R.; Hillerkuss, D.; Palmer, R.; Zwick, T.; Koos, C.; Freude, W.; Ambacher, O.; Leuthold, J.; Kallfass, I. Wireless sub-THz communication system with high data rate. *Nat. Photonics* **2013**, *7*, 977−981.

(5) Bonaccorso, F.; Sun, Z.; Hasan, T.; Ferrari, A. C. Graphene photonics and optoelectronics. *Nat. Photonics* **2010**, *4*, 611−622.

(6) Cubukcu, E.; Kort, E. A.; Crozier, K. B.; Capasso, F. Plasmonic Laser antenna. *Appl. Phys. Lett.* **2006**, *89*, 093120.

(7) Yu, N.; Cubukcu, E.; Diehl, L.; Bour, D.; Corzine, S.; Zhu, J.; Hoefler, G.; Crozier, K. B.; Capasso, F. Bowtie plasmonic quantum cascade laser antenna. *Opt. Express* **2007**, *15*, 13272−13281.

(8) Cubukcu, E.; Capasso, F. Optical nanorod antennas as dispersive one-dimensional Fabry-Perot resonators for surface plasmons. *Appl. Phys. Lett.* **2009**, *95*, 201101.

(9) Alù, A.; Engheta, N. Input Impedance, Nanocircuit Loading, and Radiation Tuning of Optical Nanoantennas. *Phys. Rev. Lett.* **2008**, *101*, 043901.

(10) Chen, H.-T.; Padilla, W. J.; Zide, J. M. O.; Gossard, A. C.; Taylor, A. J.; Averitt, R. Active terahertz metamaterial device. *Nature* **2006**, *444*, 597−600.

(11) Toma, A.; Tuccio, S.; Prato, M.; De Donato, F.; Perucchi, A.; Di Pietro, P.; Marras, S.; Liberale, C.; Proietti Zaccaria, R.; De Angelis, F.; Manna, L.; Lupi, S.; Di Fabrizio, E.; Razzari, L. Squeezing Terahertz light into nanovolumes: Nanoantenna Enhanced Terahertz Spectroscopy (NETS) of Semiconductor Quantum Dots. *Nano Lett.* **2015**, *15*, 386−391.

(12) Watts, C. M.; Liu, X.; Padilla, W. J. Metamaterial Electromagnetic Wave Absorbers. *Adv. Mater.* **2012**, *24*, OP98−OP120.

(13) Cheng, Y. Z.; Withayachumnankul, W.; Upadhyay, A.; Headland, D.; Nie, Y.; Gong, R. Z.; Bhaskaran, M.; Sriram, S.; Abbott, D. Ultrabroadband Plasmonic Absorber for Terahertz wave. *Adv. Opt. Mater.* **2015**, *3*, 376−380.

(14) Sensale-Rodriguez, B.; Yan, R.; Kelly, M. M.; Fang, T.; Tahy, K.; Hwang, W. S.; Jena, D.; Liu, L.; Xing, H. G. Broadband Graphene Terahertz Modulators Enabled by Intraband Transitions. *Nat. Commun.* **2012**, *3*, 780.

(15) Lee, S. H.; Choi, M.; Kim, T.-T.; Lee, S.; Liu, M.; Yin, X.; Choi, H. K.; Lee, S.; Choi, C.-G.; Choi, S.-Y.; Zhang, X.; Min, B. Switching Terahertz Waves with Gate-Controlled Active Graphene Metamaterials. *Nat. Mater.* **2012**, *11*, 936−941.

(16) Yao, Y.; Kats, M. A.; Genevet, P.; Yu, N.; Song, Y.; Kong, J.; Capasso, F. Broad Electrical Tuning of Graphene-Loaded Plasmonic Antennas. *Nano Lett.* **2013**, *13*, 1257−1264.

(17) Yao, Y.; Kats, M. A.; Shankar, R.; Song, Y.; Kong, J.; Loncar, M.; Capasso, F. Wide Wavelength Tuning of Optical Antennas on Graphene with Nanosecond Response Time. *Nano Lett.* **2013**, *14*, 214−219.

(18) Valmorra, F.; Scalari, G.; Maissen, C.; Fu, W.; Schoenenberger, C.; Choi, J. W.; Park, H. G.; Beck, M.; Faist, J. Low-Bias Active Control of Terahertz Waves by Coupling Large-Area CVD Graphene to a Terahertz Metamaterial. *Nano Lett.* **2013**, *13*, 3193−3198.

(19) Luo, L.; Chatzakis, I.; Wang, J.; Niesler, F. B. P.; Wegener, M.; Koschny, T.; Soukoulis, C. M. Broadband terahertz generation from metamaterials. *Nat. Commun.* **2014**, *5*, 3055.

(20) Tong, J.; Muthee, M.; Chen, S.-Y.; Yngvesson, S. K.; Yan, J. Antenna Enhanced Graphene THz Emitter and Detector. *Nano Lett.* **2015**, *15*, 5295−5301.

(21) Withers, F.; Hardisty Bointon, T.; Craciun, M. F.; Russo, S. All-graphene Photodetectors. *ACS Nano* **2013**, *7*, 5052−5057.

(22) Cai, X.; Sushkov, A. B.; Suess, R. J.; Jadidi, M. M.; Jenkins, G. S.; Nyakiti, L. O.; Myers-Ward, R. L.; Li, S.; Yan, J.; Gaskill, D. K.; Murphy, T. E.; Drew, H. D.; Fuhrer, M. S. Sensitive room-temperature terahertz detection via the photothermoelectric effect in graphene. *Nat. Nanotechnol.* **2014**, *9*, 814−819.

(23) Luxmoore, I. J.; Gan, C. H.; Liu, P. Q.; Valmorra, F.; Li, P.; Faist, J.; Nash, G. R. Strong Coupling in the Far-Infrared between Graphene Plasmons and the Surface Optical Phonons of Silicon Dioxide. *ACS Photonics* **2014**, *1*, 1151−1155.

(24) Jadidi, M. M.; Sushkov, A. B.; Myers-Ward, R. L.; Boyd, A. K.; Daniels, K. M.; Gaskill, D. K.; Fuhrer, M. S.; Drew, H. D.; Murphy, T. E. Tunable Terahertz Hybrid Metal−Graphene Plasmons. *Nano Lett.* **2015**, *15*, 7099−7104.

(25) Degl'Innocenti, R.; Jessop, D. S.; Shah, Y. D.; Sibik, J.; Zeitler, A.; Kidambi, P.; Hofmann, S.; Beere, H. E.; Ritchie, D. A. Low-Bias Terahertz Amplitude Modulator Based on Split-Ring Resonator and Graphene. *ACS Nano* **2014**, *8*, 2548−2554.

(26) Degl'Innocenti, R.; Jessop, D. S.; Shah, Y. D.; Sibik, J.; Zeitler, A.; Kidambi, P.; Hofmann, S.; Beere, H. E.; Ritchie, D. A. Terahertz optical modulator based on metamaterial split-ring resonators and graphene. *Opt. Eng.* **2014**, *53*, 057108.

(27) Zanotto, S.; Lange, C.; Pitanti, A.; Miseikis, V.; Coletti, C.; Degl'Innocenti, R.; Baldacci, L.; Huber, R.; Tredicucci, A. Magneto-optic transmittance modulation observed in a hybrid graphene−split ring resonator terahertz metasurface. *Appl. Phys. Lett.* **2015**, *107*, 121104.

(28) Liang, G.; Hu, X.; Yu, X.; Li, L. H.; Davies, A. G.; Linfield, E. H.; Liang, H. K.; Zhang, Y.; Yu, S. F.; Wang, Q. J. Integrated Terahertz Graphene Modulator with 100% modulation depth. *ACS Photonics* **2015**, *2*, 1559−1566.

(29) Chen, H.-T.; Palit, S.; Tyler, T.; Bingham, C. M.; Zide, J. M. O.; O'Hara, J. F.; Smith, D. R.; Gossard, A. C.; Averitt, R. D.; Padilla, W. J.; Jokerst, N. M.; Taylor, A. J. Hybrid metamaterial enable fast electrical modulation of freely propagating terahertz waves. *Appl. Phys. Lett.* **2008**, *93*, 091117.

(30) Shrekenhamer, D.; Strikwerda, A. C.; Bingham, C.; Averitt, R. D.; Sonkusale, S.; Padilla, W. J. High speed terahertz modulation from metamaterials with embedded high electron mobility transistors. *Opt. Express* **2011**, *19*, 9968−9975.

(31) Sagade, A. A.; Neumaier, D.; Schall, D.; Otto, M.; Pesquera, A.; Centeno, A.; Elorza, A. Z.; Kurz, H. Highly air stable passivation of graphene based field effect devices. *Nanoscale* **2015**, *7*, 3558−3564.

DOI: 10.1021/acsphotonics.5b00672
ACS Photonics 2016, 3, 464−470